

# Geophysical Research Letters®



## RESEARCH LETTER

10.1029/2024GL111084

## ENSO and West Pacific Seasonality Driven by the South Asian Monsoon

### Key Points:

- We propose a new mechanism to explain why equatorial West Pacific SSTs peak once a year and why El Niño/Southern Oscillation is phase-locked to the seasonal cycle
- Warm air advection from the Asian Monsoon makes the West Pacific warmest in boreal fall despite incoming sunlight peaking twice a year
- The resulting seasonality of Pacific SSTs and the Walker Circulation leads to El Niño and La Niña events peaking in boreal winter

P. J. Tuckman<sup>1</sup> , Jane E. Smyth<sup>1</sup> , Jingyuan Li<sup>2,3,4</sup> , Nicholas J. Lutsko<sup>2</sup> , and John Marshall<sup>1</sup> 

<sup>1</sup>Department of Earth, Atmospheric, and Planetary Sciences, Massachusetts Institute of Technology, Cambridge, MA, USA, <sup>2</sup>Scripps Institution of Oceanography, University of California San Diego, La Jolla, CA, USA, <sup>3</sup>Department of Meteorology, Stockholm University, Stockholm, Sweden, <sup>4</sup>Bolin Centre for Climate Research, Stockholm, Sweden

### Supporting Information:

Supporting Information may be found in the online version of this article.

### Correspondence to:

P. J. Tuckman,  
[tuckman@mit.edu](mailto:tuckman@mit.edu)

### Citation:

Tuckman, P. J., Smyth, J. E., Li, J., Lutsko, N. J., & Marshall, J. (2025). ENSO and West Pacific seasonality driven by the South Asian monsoon. *Geophysical Research Letters*, 52, e2024GL111084. <https://doi.org/10.1029/2024GL111084>

Received 1 JUL 2024

Accepted 16 APR 2025

### Author Contributions:

**Conceptualization:** P. J. Tuckman  
**Funding acquisition:** Nicholas J. Lutsko, John Marshall  
**Methodology:** P. J. Tuckman  
**Project administration:** John Marshall  
**Software:** P. J. Tuckman  
**Supervision:** Nicholas J. Lutsko, John Marshall  
**Visualization:** P. J. Tuckman  
**Writing – original draft:** P. J. Tuckman  
**Writing – review & editing:** P. J. Tuckman, Jane E. Smyth, Jingyuan Li, Nicholas J. Lutsko, John Marshall

**Abstract** The equatorial Pacific exhibits a clear seasonal cycle, with West Pacific SSTs being highest during boreal autumn and El Niño/Southern Oscillation (ENSO) events tending to peak during boreal winter. In this work, we use the concept of a monsoonal mode and idealized coupled simulations to show that the presence of a large land mass in the Northern Hemisphere can lead to these seasonal asymmetries. Specifically, warm air moving east from the Asian summer monsoon suppresses surface fluxes in the West Pacific, leading to increased temperature there during the following months. The warmth of the West Pacific in boreal autumn strengthens the Walker circulation and the zonal temperature gradient across the Pacific, leading to the growth of El Niño events during that season. In summary, the presence of the Asian monsoon north of the equator results in ENSO events preferentially growing during boreal autumn and peaking during boreal winter.

**Plain Language Summary** El Niño events, characterized by warming of the central and eastern equatorial Pacific, are a major driver of interannual variability around the globe. Despite solar insolation peaking twice per year on the equator, El Niño events are almost always strongest during boreal winter. In this work, we show that the presence of Asia in the Northern Hemisphere leads to this seasonality. Specifically, warm air blowing east from the South Asian monsoon during boreal summer warms the West Pacific. This makes the West Pacific warmest during boreal fall, which serves as a supply of energy for El Niño events to grow during that season and peak during boreal winter.

## 1. Introduction

The equatorial Pacific and the El Niño/Southern Oscillation (ENSO) display seasonal cycles that favor one season, despite solar insolation peaking twice a year on the equator. West Pacific Sea Surface Temperatures (SST, Figure 1a) are roughly constant throughout June-July-August (JJA), increase during September-October-November (SON), decrease during December-January-February (DJF), and increase again during March-April-May (MAM). Meanwhile, the East Pacific (panel b) has an opposite seasonal cycle with larger amplitude, being coldest during SON and warmest during MAM. If the temperature of the equatorial Pacific were controlled only by incoming solar radiation, both these seasonal cycles would have two maxima associated with peak insolation crossing the equator twice a year, yet they each have only one. In other words, on the equator, one might expect boreal spring/summer to be the same as fall/winter, yet the West Pacific is warmer in October, while the East Pacific is warmer in April (Figure 1c, see Figure S1 in Supporting Information S1 for the full Pacific seasonal cycle).

ENSO also exhibits strong seasonality, despite being an interannual phenomenon with a period of 3–6 years. For example, the 1997–1998 El Niño event had a clear signal in June (Figure 1d), strengthened considerably during SON, and peaked in December (Figure 1e). Between 1959 and 2021 almost all ENSO events peaked during DJF, while none peaked during JJA (Figure 1f). In this work, we propose a novel and intuitive explanation for this seasonal asymmetry: warm air blowing eastward from the South Asian monsoon into the West Pacific suppresses heat loss and increases the temperature there during boreal autumn. The warm West Pacific favors ENSO growth, leading to El Niño events peaking during boreal winter.

The tropical Pacific is of outsized importance in global climate due to ENSO (Battisti & Sarachik, 1995; Clarke, 2014; Philander et al., 1984; Timmermann et al., 2018), which impacts worldwide weather (Hoerling et al., 1997; Neelin et al., 2003; Zhou et al., 2014) and SSTs (Johnson & Birnbaum, 2017). Previous work on

© 2025. The Author(s).

This is an open access article under the terms of the [Creative Commons Attribution License](https://creativecommons.org/licenses/by/4.0/), which permits use, distribution and reproduction in any medium, provided the original work is properly cited.

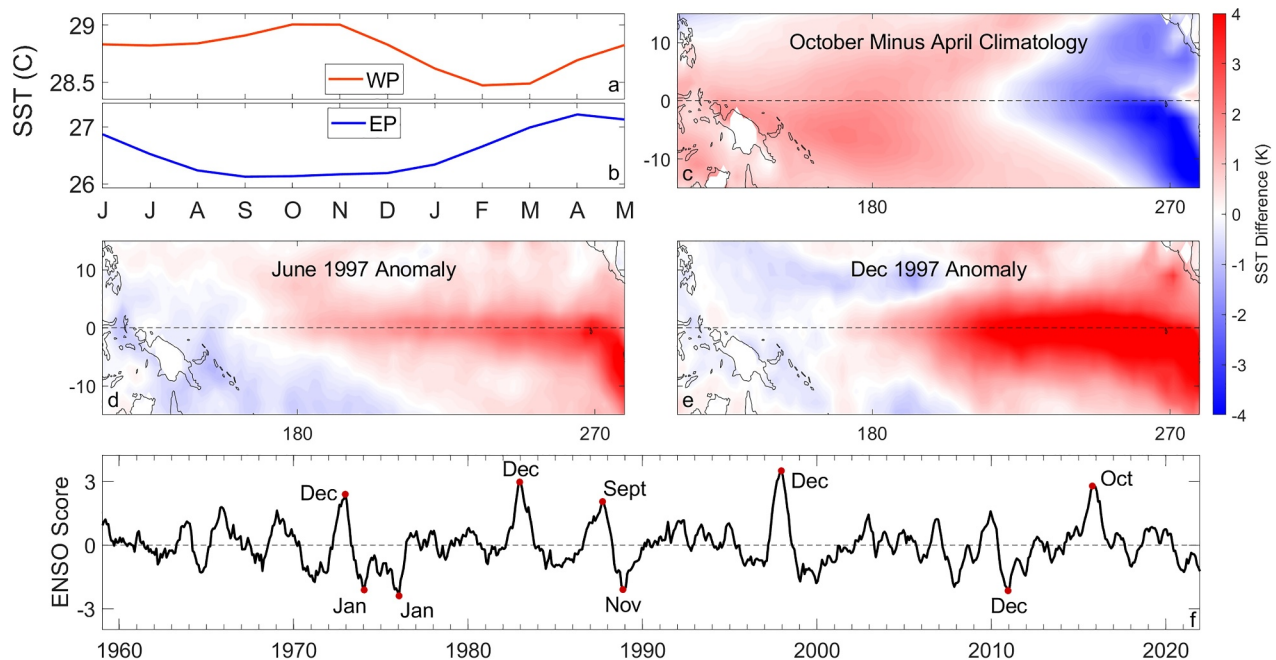


**Figure 1.** (a) The seasonal cycle of West Pacific (160–190°E, 15°N–15°S) and (b) East Pacific (235–260°E, 15°N–15°S) SSTs from ERA5 Reanalysis, (c) the difference in SST between the October and April climatology (zonal mean removed), and (d) June and (e) December SST anomalies during the growth of the 1997 El Niño event. (f) A detrended time series of El Niño/Southern Oscillation score, defined as the first principal component of interannual variability of tropical SSTs. The months of the positive and negative peaks of normalized amplitude larger than two are labeled.

ENSO, using methods ranging from simplified analytic models (Burgers et al., 2005; Jin, 1998) to intermediate complexity models (Jin et al., 2006) and full general circulation models (GCMs, Delecluse et al., 1998; Guilyardi, 2006; Guilyardi et al., 2009; Philander et al., 1992), has found that ENSO's seasonality is set by El Niño growth rates, which are highest during SON (Chen & Jin, 2020, 2022; S.-K. Kim & An, 2021; Stein et al., 2014). Tziperman et al. (1997) further showed, using the Zebiak and Cane ENSO model (Zebiak & Cane, 1987), that these growth rates are controlled by the background seasonality of the Pacific, especially the wind divergence and SSTs. However, there is little consensus about what drives these seasonal asymmetries, and therefore the fundamental reason for ENSO events peaking during DJF.

The best known explanation for the seasonal asymmetry of East Pacific wind divergence, and therefore ENSO, is the annual mean position of the Intertropical Convergence Zone (ITCZ). Specifically, because the annual mean ITCZ is in the Northern Hemisphere, trade winds are strongest when the ITCZ is farthest north, that is, in JJA and SON. ENSO growth rates are therefore enhanced in those seasons, leading to ENSO events peaking in DJF (Li & Philander, 1996; Tziperman et al., 1997). Various explanations have been suggested for the asymmetry of the annual mean ITCZ, including the Atlantic Meridional Overturning Circulation transporting energy northward (Green et al., 2017; Moreno-Chamarro et al., 2020), and the slant of South America (Philander et al., 1996).

Another suggested explanation for the seasonal asymmetry of ENSO is the precession of Earth's orbit. The anomalous insolation during Earth's perihelion can cause seasonal asymmetries in the Pacific, although models differ on the details and magnitude of this effect (Chiang & Broccoli, 2023; Erb et al., 2015; Lu & Liu, 2019).

The seasonality of the West Pacific warm pool has also been extensively studied (Chang, 1994; Clement et al., 2005; DeWitt & Schneider, 1999; S. T. Kim et al., 2012; Köberle & Philander, 1994; E. K. Schneider, 2002; Y. Wang et al., 2019; Yin et al., 2020). Previous research has identified proximate causes of seasonal asymmetry, such as net surface heat fluxes (N. Schneider et al., 1996; W. Wang & McPhaden, 1999) and wind-forced Kelvin and Rossby waves (Yu & McPhaden, 1999), but not a fundamental reason for fall and spring being different on the equator.

Here, we argue that the seasonality of the tropical Pacific and therefore of ENSO is a result of the presence of the South Asian monsoon. We use the concept of the Indo-Pacific monsoonal mode introduced in Tuckman

et al. (2024) as a framework; warm air blowing eastward from Asia during JJA suppresses surface fluxes in the West Pacific, enhancing SSTs and, therefore, the Pacific temperature gradient during SON. This strengthens the Walker circulation, creating a seasonality in low-level winds, which, together with the seasonality of SSTs, phase locks ENSO to the seasonal cycle. To isolate key processes, we run idealized coupled simulations with two simplified continental configurations, one with a representation of Asia and one without. Only in the presence of Asia, and therefore a monsoon, do the equatorial Pacific and ENSO have seasonal cycles that match observations.

## 2. Methods

We use ERA5 atmospheric reanalysis (Hersbach et al., 2020) and idealized coupled atmosphere-ocean experiments to isolate and understand the role of the Asian Monsoon in tropical Pacific seasonality. The models consist of an idealized, moist atmosphere with gray radiation and a dynamic ocean, with barriers separating the Pacific, Atlantic, and Indian basins (Marshall et al., 1997; Tuckman et al., 2024). We compare two simulations: a “continent” simulation in which Eurasia is represented as a wide mid-latitude region with reduced heat capacity and no ocean dynamics; and an “aquaplanet” simulation with no representation of land (Figure 2). The idealized continent produces intense precipitation during JJA, analogous to the South Asian monsoon, whereas the aquaplanet simulation does not. Further details of the model setup are found in the Appendix A, and relevant diagnostic quantities are shown in Figures S2 and S3 in Supporting Information S1.

In both simulations, the first principal component of interannual variability in tropical ocean temperatures resembles the observed ENSO mode (Figure 2, right column). This mode shows warming of the central and eastern equatorial Pacific, cooling of the western Pacific, and explains 25%–35% of interannual variability in the tropics. The regions to be studied are highlighted with orange (West Pacific) and blue boxes (East Pacific). These areas are chosen to be representative of the West Pacific warm pool and the East Pacific cold tongue, respectively. We analyze potential temperature at 25 m depth (hereafter  $T_{25}$ ) for the simulations as it is less noisy and a better metric of ocean heat content than SST, while for reanalysis we use SST as it is the most readily available variable. Additionally, the simulations have upwelling along the eastern boundary of the Pacific, which affects the SST, but not  $T_{25}$ . The simulations' ENSO modes have roughly similar periods to the observed ENSO mode (bottom of Figure 2), whose broad power spectrum peaks between 3 and 6 years. The modeled power spectra peak at 4 and 5 years in the aquaplanet and continent simulations, respectively; both are within the error bounds of the observed power spectrum. The difference in the period of ENSO between the simulations could be due to the presence of a continent influencing teleconnections between the Indian and Pacific Oceans (further discussed in Appendix A). Most importantly, both models simulate realistic interannual variability in the Pacific, giving confidence in their use for studying ENSO.

## 3. Pacific Seasonality With and Without a Monsoon

The seasonality of the equatorial Pacific is captured in the continent simulation but not in the aquaplanet simulation (Figure 3). West Pacific temperatures in reanalysis (panel a) peak in SON and have a minimum in February. The  $T_{25}$  from the continent simulation is comparable, peaking in October and November and having a minimum in February and March. The aquaplanet simulation, however, has a roughly symmetric seasonal cycle, with maxima during both solstitial seasons. In the East Pacific (panel b), both reanalysis and the continent simulations are warmest in MAM and coldest in SON, while the aquaplanet simulation once again has two maxima and two minima over the course of the year. Without a continent to break the hemispheric symmetry (i.e., in the aquaplanet simulation), there is little difference between summer and winter along the equator. Note that the simulations show a larger seasonal cycle of temperature in the West Pacific than does reanalysis, likely due to model idealizations (such as the lack of clouds and atmospheric short-wave absorption) or model biases in the mixed layer depth.

Next, we compare the simulated seasonal distribution of ENSO peaks with that of reanalysis (Figure 3c). An ENSO peak is defined as an East Pacific temperature which exceeds the mean for that time of year by two standard deviations and is at its highest within a 12 months window. The threshold for reanalysis is one standard deviation, as it is a shorter time series. In observations, more than 65% of ENSO peaks occur in DJF, while less than 10% occur during JJA. ENSO seasonality in the continent simulation is similar, with 64% of the peaks being during DJF and 11% in JJA. By contrast, in the aquaplanet simulation, there is little seasonality, with slightly more peaks during JJA or DJF and fewer during SON or MAM.

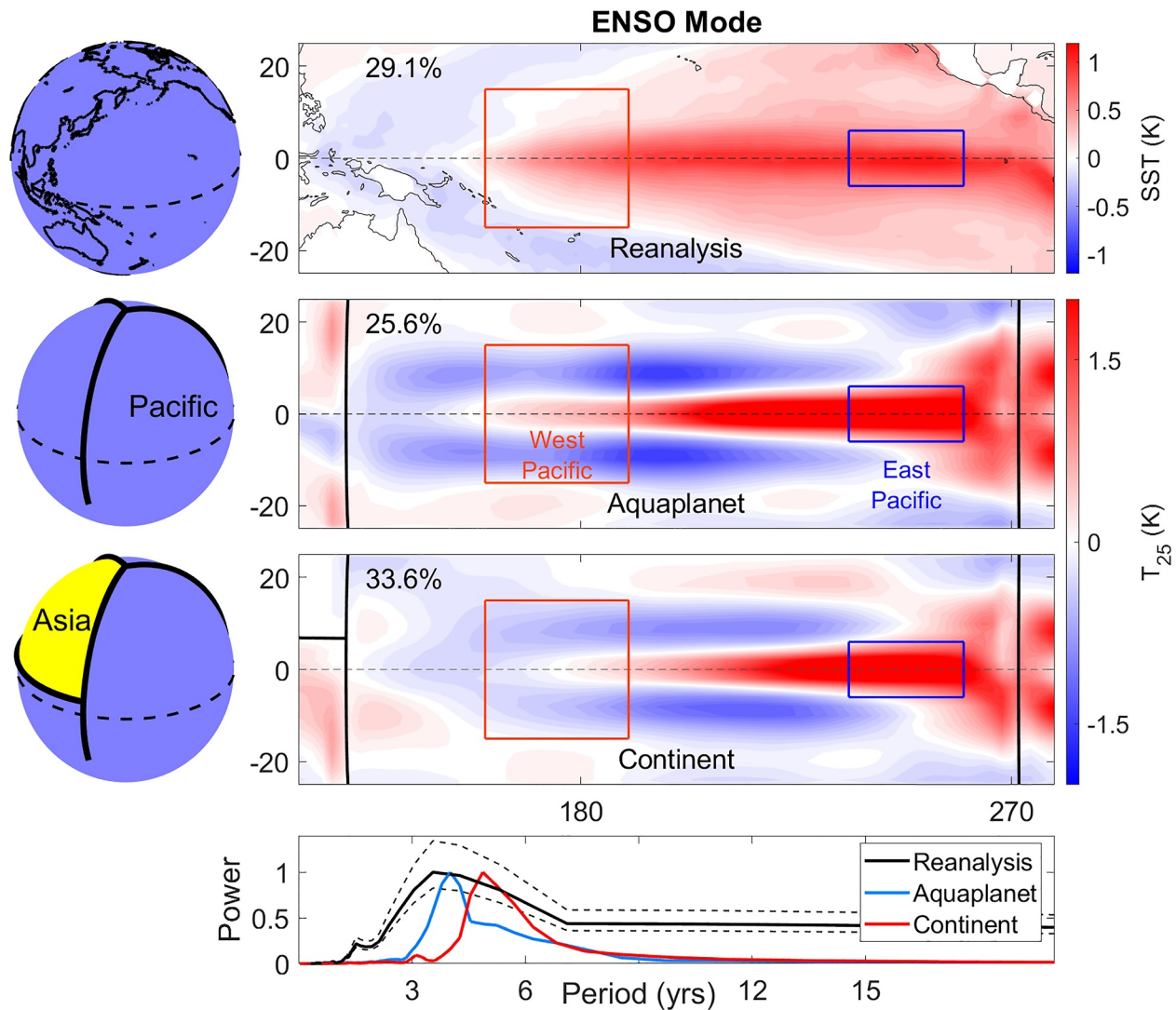


**Figure 2.** (left) Continental configuration and (right) the El Niño/Southern Oscillation (ENSO) mode, calculated as the first principal component of tropical interannual variability for (top) reanalysis data, (middle) the “aquaplanet” and (bottom) “continent” simulations. Asia reaches from 0° to 135°E and from 8° to 90°N in the continent simulation, and the thin barriers are at 0°, 135°, and 270°E in both simulations. The fraction of variability explained is shown in the top left of each panel. (bottom) The power spectra of the ENSO mode in each case, with a 50% confidence interval plotted as thin dashed lines for reanalysis. Rectangular boxes indicate regions which are representative of the West Pacific (orange, 160–190°E, 15°N–15°S) and East Pacific (blue, 240–265°E, 5°N–5°S). The ENSO mode is calculated from reanalysis SSTs and from potential temperature 25 m below the surface ( $T_{25}$ ) in the simulations.

In summary, the continent simulation broadly captures the seasonality of the equatorial Pacific, both in its climatology and interannual variability, while the aquaplanet simulation does not. This strongly suggests that the presence of Asia plays an important role in the seasonality of the Pacific, which we now explain using the concept of a monsoonal mode.

### 3.1. Role of the Monsoonal Mode

Observations show that an atmospheric energy and precipitation anomaly forms over South Asia in boreal spring/summer due to excess heating over land. This anomaly is then advected eastward into the West Pacific in boreal autumn and remains there due to interactions with the East Pacific cold tongue and equatorial easterlies. Tuckman et al. (2024) interpreted this phenomenon as a “monsoonal mode”: A zonally propagating moist energy anomaly of continental and seasonal scale. This provides a framework for understanding how the South Asian monsoon influences the seasonal cycle of the West Pacific and ENSO (Figure 4).

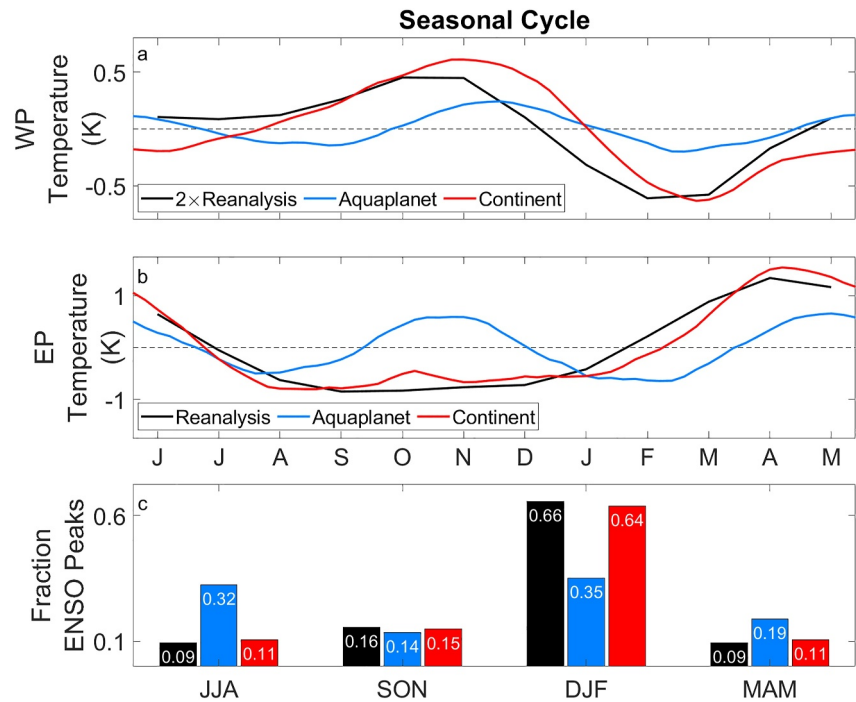


**Figure 3.** The seasonality of the equatorial Pacific. Panel (a) shows the seasonal cycle of West Pacific (orange box from Figure 2) reanalysis SST (black) and potential temperature 25 m below the surface ( $T_{25}$ ) from the aquaplanet simulation (blue) and continent simulation (red). Panel (b) shows the same for the East Pacific (blue box from Figure 2). Panel (c) shows the fraction of El Niño/Southern Oscillation (ENSO) peaks that occur in each season for reanalysis (black), the aquaplanet simulation (blue), and the continent simulation (red). The reanalysis SST in panel a is multiplied by two so that the amplitude is similar to that of  $T_{25}$  from the continent simulation, and the reanalysis ENSO score is smoothed with a 2 month moving mean to decrease noise.

The monsoonal mode is most clearly visible in the seasonality of the energy flux potential (EFP), defined such that its gradient is the atmospheric moist energy transport (see Appendix A for details, Boos & Korty, 2016). Figure 4 shows the seasonal cycle of the EFP maxima, the region from which energy is exported meridionally and zonally, in (a) reanalysis, (b) the aquaplanet simulation, and (c) the continent simulation. In reanalysis and the continent simulation, energy is exported from Southern Asia/the Northern Indian Ocean during JJA and from the equatorial West Pacific during DJF. However, in the aquaplanet simulation, there is only a small maximum EFP over the Western Indian Ocean with little seasonal movement. There is also an EFP maximum over the Western Pacific in the aquaplanet simulation, as the Pacific and Indian basins are similar (not shown in Figure 4, see Figure S3 in Supporting Information S1).

The monsoonal mode mechanism and its relevance is demonstrated on the right side of Figure 4. A continent in the Northern Hemisphere (panel d, gray) becomes very warm during JJA due to its low heat capacity, leading to large energy fluxes from the land surface (orange arrows) and an EFP maximum (green circle). The energetic air above the continent is advected eastward by the monsoon winds (black arrow), leading to anomalously warm and humid air over a cool surface. This suppresses surface fluxes (red arrows), leading to less energy leaving the West Pacific in the continent simulation than in the aquaplanet simulation from May to September (panel e). Consequently, the West Pacific is warmer in the continent simulation during SON (panel f). In other words, warm air moving east from Asia during JJA suppresses surface fluxes in the West Pacific, causing ocean temperatures there to peak in SON, as seen in Figure 3a. It is important to note that surface fluxes are affected by wind speeds as well as air-sea temperature differences, but the wind speeds in the two simulations are very similar during the relevant season (Figure S4 in Supporting Information S1).

Although the EFP indicates the presence of a monsoonal mode in reanalysis and the continent simulation, there are factors that complicate our interpretation. First, the use of monthly EFPs can give the impression that the movement of the mode from Southern Asia to the West Pacific is discontinuous, while it is in fact smooth. This is shown in detail in Tuckman et al. (2024), and can be seen in reanalysis precipitation (Figure S5 in Supporting

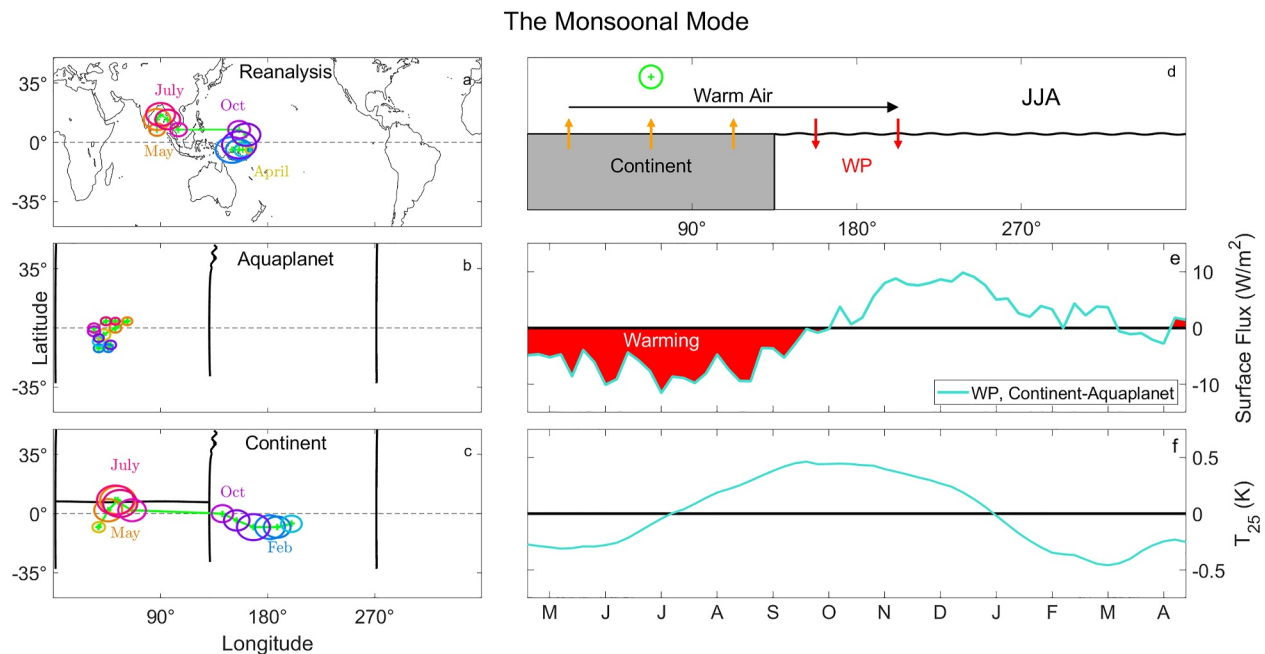


**Figure 4.** Elements of the monsoonal mode. The seasonal cycle of the energy flux potential (EFP) maximum in (a) reanalysis, (b) the aquaplanet, and (c) the continent simulations. The color of the circle changes each month, and its radius is a measure of the strength of zonal heat transport. The monthly positions of the EFP maxima are connected with a green line (in panels a and c). (d) A schematic of the monsoonal mode in JJA. (e) The difference in West Pacific surface flux between the continent and aquaplanet simulations over the seasonal cycle. (f) The difference in West Pacific  $T_{25}$  between the continent and aquaplanet simulations.

Information S1). Additionally, there are some notable biases in the continent simulation, including a westward shift in boreal summer and eastward movement in boreal winter. These are likely due to our use of a simplified continental configuration without a representation of Africa or Australia, which influence the boreal summer and winter EFPs, respectively.

The seasonality of the East Pacific SST is also controlled by the presence of a continent, through a combination of the monsoonal mode and the Bjerknes feedback (Bjerknes, 1969). Specifically, the warmer continent/West Pacific in boreal summer and fall enhances the strength of the Walker circulation, and therefore the westward current (Figure S6a in Supporting Information S1) and upwelling (Figure S6b in Supporting Information S1) in the East Pacific. This cools the East Pacific by exporting warm water to the west (Figure S6c in Supporting Information S1) and bringing cold water toward the surface from below (Figure S6d in Supporting Information S1). In other words, the Walker circulation being strongest in boreal summer and fall cools the East Pacific during JJA and makes it coldest during SON (Figure 3b). By contrast, the cooler West Pacific in DJF and MAM dampens the Walker circulation, warming the East Pacific. In the aquaplanet simulation, the Walker circulation has little seasonality, leading to summer/winter and fall/spring symmetry of East Pacific temperatures.

In summary, warm air moving east from Asia during JJA suppresses surface fluxes in the West Pacific, causing temperatures there to peak in SON, as seen in Figure 3a. The warmer West Pacific in SON also strengthens the Walker circulation, which (a) further warms the West Pacific by preventing upwelling there and (b) cools the cold tongue (Bjerknes, 1969), causing the East Pacific to have the opposite seasonality as the West Pacific (Figure 3b). We now turn to how this background Pacific seasonality interacts with ENSO.

### 3.2. Seasonality of ENSO

To explore the processes that influence ENSO seasonality, we use a modified Bjerknes index (Jin et al., 2006, 2020) to calculate an ENSO growth rate. The real part of the Bjerknes index (a measure of ENSO growth) depends on changes in the near-surface temperature of the East Pacific and the relaxation of the West Pacific thermocline (Jin et al., 2020), so we quantify these two factors. For the East Pacific temperature, we diagnose a linearized anomalous temperature budget of the mixed layer in the equatorial Central and Eastern Pacific (190°–260°E, 5°S–5°N, 0–80 m depth):

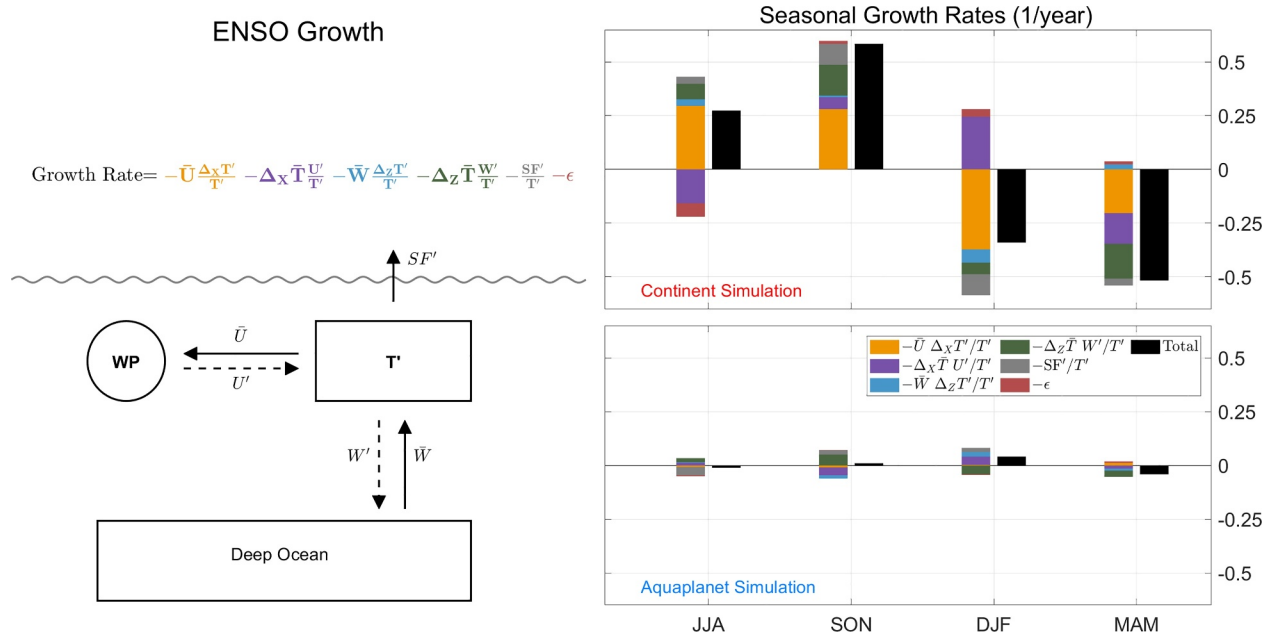


**Figure 5.** Exploring processes that control simulated El Niño/Southern Oscillation growth rates over the seasonal cycle. The equation on the left shows how ENSO growth rates depend on advection, surface fluxes, and West Pacific thermocline depth relaxation ( $\epsilon$ ), while the bottom shows a schematic of the Central-East Pacific ( $190^{\circ}$ – $260^{\circ}$ E) energy budget and terms contributing to it. Arrows indicate current direction, overbars and solid arrows indicate the climatological seasonal cycle, while primes and dashed arrows indicate anomalies. The right side shows the seasonality of growth rates in the (top) continent and (bottom) aquaplanet simulations: the black bar is the total growth rate and its components are in colors. All growth terms are computed as the difference from the annual mean. Note that the total growth rate includes contributions from meridional advection, which are not shown directly here. More details can be found in Appendix A.

$$\frac{1}{T'} \frac{\partial}{\partial t} T' \approx -\frac{\Delta_x T'}{T'} \bar{U} - \frac{U'}{T'} \Delta_x \bar{T} - \frac{\Delta_z T'}{T'} \bar{W} - \frac{W'}{T'} \Delta_z \bar{T} - \frac{1}{T'} SF', \quad (1)$$

where  $T$  is temperature,  $U$  is the zonal current,  $W$  is the vertical current, and  $SF$  is the surface flux (schematic on left side of Figure 5). The overbars denote the climatological seasonal cycle, the primes denote anomalies from the seasonal cycle, and  $\Delta_x$  and  $\Delta_z$  indicate finite differences in the zonal and vertical directions across the box studied. We neglect nonlinear terms, meridional advection, and anomalous sources or sinks besides surface fluxes. Each term has been divided by  $T'$ , so it can be interpreted as a contribution to the total growth rate of an El Niño or La Niña event once the event begins (i.e.,  $T' \neq 0$ ).

Meanwhile, the West Pacific thermocline relaxation (represented as  $\epsilon$ ) is calculated directly from the simulations as the slope of the line of best fit between  $h_w$  and  $dh_w/dt$ , where  $h_w$  is the anomalous depth of the West Pacific thermocline (further details can be found in the Appendix A).

The seasonal contributions of each term to ENSO growth are shown on the right side of Figure 5 for the continent (top) and the aquaplanet simulations (bottom). The total growth rate for the continent simulation (black bars) is positive in JJA, peaks in SON, and is negative in DJF and MAM. This seasonality is primarily determined by the mean zonal current acting on the anomalous temperature (orange), with secondary contributions from the anomalous zonal current acting on the mean temperature (purple), the mean stratification (green), and surface fluxes (grey). All of these quantities are affected by the monsoonal mode through the modulation of Pacific surface temperatures and related currents. As discussed above, the presence of a continent leads to a seasonality in the Walker circulation, and therefore the near-surface westward current (Figure S6a in Supporting Information S1) and East Pacific upwelling (Figure S6b in Supporting Information S1). This strengthens the Pacific temperature gradient in JJA and SON, leading to enhanced ENSO growth in those seasons. The cooler West Pacific in DJF and MAM dampens the Walker circulation and East Pacific upwelling, which warms the water at the bottom of the mixed layer. These factors influence ENSO growth rates through  $\Delta_x \bar{T}$  (purple),  $\bar{U}$  (orange), and  $\Delta_z \bar{T}$  (green), shown on the right side of Figure 5. Intuitively, since the Walker circulation/cold tongue feedback is

the source of ENSO instability, the system is most unstable when these features are strongest in SON and most stable when they are weakest in MAM.

Surface fluxes also slightly amplify the seasonal cycle of ENSO growth, mostly through the temperature of the East Pacific. Despite model simplifications, the relative importance of these terms, and specifically the dominance of zonal advection in setting the seasonality of ENSO, is in agreement with previous work (Chen & Jin, 2022). The effect of surface fluxes in our model is small, which may be due to equatorial winds associated with the ITCZ having a too small seasonal cycle. Thermocline relaxation ( $\epsilon$ ) and mean upwelling acting on the anomalous temperature gradient ( $\bar{W}\Delta_z T'/T'$ ) do not have significant seasonal cycles.

For the aquaplanet simulation (bottom right of Figure 5 and blue lines in Figure S6 in Supporting Information S1), the ENSO growth rate and its components have small seasonal cycles, leading to little seasonality in ENSO peaks (Figure 3). Note that the growth rates are displayed here with the annual means removed; the two simulations' absolute growth rates (which are similar) and the corresponding ENSO time series are shown in Figure S7 in Supporting Information S1.

In the presence of a continent, the transition from growth to decay in DJF causes ENSO events to peak in that season. The growth rates are controlled mostly by variations in the zonal current and the zonal temperature gradient, since the relationship between these (i.e., the Bjerknes feedback) is the source of ENSO instability. The presence of a continent north of the equator explains this seasonality, as the monsoonal mode induces seasonal cycles in the temperature of the equatorial Pacific and the strength of the Walker circulation.

#### 4. Conclusions

We have proposed a simple explanation for the seasonality of the equatorial Pacific and the seasonal phase-locking of ENSO. That the West Pacific is warmest during SON and that ENSO events peak during DJF can both be understood as consequences of the annual Indo-Pacific monsoonal mode, in which warm air moving eastward from the Asian Monsoon suppresses surface fluxes in the West Pacific (Tuckman et al., 2024). In our aquaplanet simulation, which does not have a continent or a monsoon, the West Pacific has little spring/autumn asymmetry, and ENSO events peak during boreal summer just as often as in boreal winter. However, when a monsoon is present, the West Pacific is warmest during SON and ENSO events peak during boreal winter, just as in observations. The seasonality of ENSO stems from the impact of the monsoonal mode on the zonal temperature gradient across the Pacific and associated changes in the Walker Circulation.

Our study shows that the presence of Asia and its annual monsoon is a sufficient condition to capture the major seasonal asymmetries in the equatorial Pacific. However, it may not be a necessary condition, as there are other sources of hemispheric asymmetry on Earth. These include the Andes (Baldwin et al., 2021; Takahashi & Battisti, 2007a, 2007b), the Atlantic Meridional Overturning Circulation (Marshall et al., 2014), the precession of Earth's orbit (Lu & Liu, 2019), and the slant of South America (Li & Philander, 1996; Philander et al., 1996), all of which may break the seasonal symmetry of the equatorial Pacific. However, the influence of the monsoon considered here is an intuitive explanation of ENSO seasonality and incorporates an understanding of the spring/autumn asymmetry in the West Pacific. Additionally, none of the above mechanisms can explain the results shown here, as in our two simulations the ITCZs are similar (Figure S8 in Supporting Information S1), South America is not tilted, the Andes are not represented, and Earth's orbit is circular. Further studies with idealized configurations could be designed to explore the influence of each of these effects.

Our results have important implications for understanding the equatorial Pacific. First, they directly relate properties of the tropical Pacific to those of Asia and the South Asian monsoon. This means that studying the Pacific requires accounting for the influence of the monsoonal mode. The interannual variability of the monsoon and the modulation of the monsoonal mode by continental drift on geological timescales may substantially influence the equatorial Pacific. The monsoon-ENSO connection also suggests a framework in which to analyze model biases in ENSO seasonality (Bellenger et al., 2014; Liu et al., 2021; Tian et al., 2019). Such biases could be due to model differences in the strength or movement of the monsoonal mode. Second, any insight into ENSO seasonality may have implications for the spring ENSO predictability barrier (SPB, Duan & Wei, 2013; Levine & McPhaden, 2015). The ENSO state helps initialize seasonal predictions, so negative ENSO growth rates in MAM make it more difficult to predict the climate in the following months. The framework of the monsoonal mode suggests a simple and intuitive reason for the SPB: negative ENSO growth rates in the spring, caused by a

weakened Walker Circulation and a small zonal temperature gradient across the Pacific, are due to the presence of a large continent in the Northern Hemisphere. By connecting the seasonality of ENSO to the presence of Asia, we have made progress toward understanding the fundamental predictability of the Earth system.

## Appendix A

In this appendix, we discuss the coupled simulations used, the calculation of the energy flux potential shown in Figure 4, the use of reanalysis data, and the ENSO energy budget discussed in reference to Figure 5.

### A1. Coupled Model Simulations

The coupled atmosphere-ocean simulations used in this study are similar to those described in Tuckman et al. (2024) based on the MITgcm (Marshall et al., 1997). The code is available at [https://github.com/MITgcm/verification\\_other/tree/master/cpl\\_gray%2Bswamp%2Bocn](https://github.com/MITgcm/verification_other/tree/master/cpl_gray%2Bswamp%2Bocn). Simulations are run for at least 750 years to ensure that the coupled system achieves a quasi-steady state. Diagnostics are averaged over the final 100 years, except in the calculation of ENSO statistics (i.e., Figures 2 and 3c), which uses 200 years to minimize noise.

The model employs identical cubed-sphere grids representing the atmosphere and ocean with  $\sim 2.8^\circ$  horizontal resolution in the tropics (Adcroft et al., 2004). The atmosphere has 26 vertical levels, idealized moist physics, a gray radiation scheme (Frierson et al., 2007), and water vapor feedback on long-wave optical thickness (Byrne & O’Gorman, 2013). There are no clouds or shortwave absorption in the atmosphere. The model employs a seasonal cycle of solar radiation appropriate for a circular orbit with an obliquity of  $23.45^\circ$ .

The dynamic ocean has 43 vertical levels with a uniform depth of 3.4 km and uses the mixing scheme developed in Gaspar et al. (1990). The continent simulation has three infinitesimally thin ridges running south from the North Pole and a large landmass, treated as a 2 m slab ocean (globe in Figure 2), extending from roughly  $8^\circ\text{N}$  to the North Pole. The landmass represents Asia, two thin barriers stretching from the North Pole to  $35^\circ\text{S}$  demarcate the Atlantic basin, and one reaching  $30^\circ\text{S}$  separates the Indian and Pacific oceans. In order to conserve freshwater, excess water that precipitates over the continent is redirected into the Atlantic basin. The aquaplanet simulation has the same three north-south boundaries but has no representation of Asia.

Both simulations have a West Pacific warm pool and an East Pacific cold tongue comparable to reanalysis, despite the highly idealized model (Figures S2 and S3 in Supporting Information S1). The simulated surface winds exhibit an Inter-Tropical Convergence Zone, tropical easterlies, and extratropical westerlies (as shown in Tuckman et al. (2024), Figure 3). It should be noted that the simulations' ENSO patterns feature a negative signal in the equatorial Atlantic, and strong teleconnections with the Indian Basin (Figure S9 in Supporting Information S1). This is likely due to ENSO teleconnections between basins that are delineated by thin barriers. It is not obvious why the ENSO mode is in the Pacific, rather than the Indian basin, as they are the same width. In the continent simulation, the presence of a continent likely interferes with the development of ENSO events, while in the aquaplanet simulation, being westward of the smallest basin (i.e., the Atlantic), seems to favor ENSO instability. Both the teleconnection to the Atlantic basin and the lack of an Indian ocean ENSO are not relevant to our focus here.

### A2. The Energy Flux Potential and Reanalysis Data

We calculate an EFP  $\chi$  (Boos & Korty, 2016), which is a solution to:

$$\nabla^2 \chi = -\vec{\nabla} \cdot \langle h\vec{u} \rangle, \quad (\text{A1})$$

where  $\nabla^2$  is the 2D Laplacian acting on a scalar,  $\vec{\nabla} \cdot$  is the 2D divergence, and  $\langle h\vec{u} \rangle$  is the vertically integrated horizontal transport of moist static energy (MSE), defined as:

$$h = Lq + gz + c_p T, \quad (\text{A2})$$

where  $q$  is specific humidity,  $z$  is height,  $T$  is temperature, and the constants  $L \equiv 2.25 \times 10^3$  kJ/kg,  $g \equiv 9.8$  m/s<sup>2</sup>, and  $c_p \equiv 1005$  J/kg/K are the latent heat of vapourization of water, the acceleration due to gravity, and the specific heat of air at constant pressure.

We use monthly mean SSTs from the ERA5 global atmospheric reanalysis produced by ECMWF (Hersbach et al., 2020) and the mass-corrected divergence of total energy (Mayer et al., 2022), with resolutions of 0.25°. The divergence includes a component from the kinetic energy, although this contribution is negligible compared to the MSE described above. The EFP data are averaged from 1979 to 2020 to calculate the climatological means, while the SST data are averaged from 1959 to 2021.

The ENSO score in reanalysis (Figure 1) is defined as the normalized mean SST in the East Pacific box shown in Figure 2. Normalization consists of taking the detrended values, subtracting the mean value for each time of year, and then dividing by the standard deviation of the resulting time series.

### A3. Energy Budget and ENSO Growth Rates

We use an ocean energy budget applied to the Central-Eastern Pacific to understand how the growth of an ENSO event is modulated by the seasonal cycle. We write an ocean temperature budget:

$$\frac{\partial T}{\partial t} + U \frac{\partial T}{\partial x} + V \frac{\partial T}{\partial y} + W \frac{\partial T}{\partial z} = S_i - S_o \quad (\text{A3})$$

where  $T$  is the temperature as a function of position  $(x,y,z)$  and time  $(t)$ , temperature is advected by the currents  $(U, V,W)$ , and source and sink terms are summarized as  $S_i$  and  $S_o$ , respectively. We focus on the near-surface equatorial central and eastern Pacific (190°–260°E, 5°S–5°N, 0–80 m depth). This is chosen to monitor the anomalous temperature of the East Pacific, but extends through the Central Pacific so that ENSO seasonality can be directly related to the monsoonal mode through the West Pacific temperature.

Terms are evaluated using finite differences to approximate the spatial derivatives, and the temperature budget can then be written:

$$\frac{\partial T}{\partial t} + U \Delta_x T + V \Delta_y T + W \Delta_z T = S_i - S_o$$

where all quantities are averaged over our chosen region. We now split each term (e.g.,  $T$ ) into a climatological seasonal cycle ( $\bar{T}$ ) and an anomaly from this seasonal cycle ( $T'$ ). We will assume that the only relevant source or sink is the surface flux, which in the mean is simply  $\overline{SF}$  and in the anomaly we will represent as  $SF' = \bar{\alpha}T'$ , where  $\bar{\alpha}$  changes over the seasonal cycle. This yields a temperature budget for the mean seasonality:

$$\frac{\partial \bar{T}}{\partial t} = -\bar{U} \Delta_x \bar{T} - \bar{V} \Delta_y \bar{T} - \bar{W} \Delta_z \bar{T} - \overline{SF}$$

and anomalies from it:

$$\begin{aligned} \frac{\partial T'}{\partial t} = & -\bar{U} \Delta_x T' - U' \Delta_x \bar{T} - U' \Delta_x T' \\ & -\bar{V} \Delta_y T' - V' \Delta_y \bar{T} - V' \Delta_y T' \\ & -\bar{W} \Delta_z T' - W' \Delta_z \bar{T} - W' \Delta_z T' \\ & -\bar{\alpha}T', \end{aligned}$$

We are interested in how an El Niño anomaly, that is, a positive value of  $T'$ , is influenced by the climatological seasonal cycle, that is,  $\bar{\alpha}$ ,  $\bar{T}$ ,  $\bar{U}$ ,  $\bar{V}$  and  $\bar{W}$ . The relevant terms are therefore those that are the product of a mean and an anomaly quantity, such as  $\bar{U} \Delta_x T'$ ,  $U' \Delta_x \bar{T}$ , etc. Previous work has shown that the relevant terms for the growth of El Niño events, especially with regard to the seasonal cycle, are zonal and vertical advection and surface fluxes (An & Jin, 2004; Chen & Jin, 2022; Tziperman et al., 1997; Vallis, 1988), supporting the neglect of other source and sink terms. We also neglect meridional advection, as its contribution is small.

Five terms remain: (a) The mean horizontal current acting on the anomalous temperature, (b) the anomalous horizontal current acting on the mean temperature, (c) the anomalous vertical current acting on the mean

temperature, (d) the mean vertical current acting on the anomalous temperature, and (e) surface fluxes. Dividing by  $T'$  to obtain quantities with units of inverse time (i.e., a growth rate), we can write:

$$\frac{1}{T'} \frac{\partial}{\partial t} T' = -\frac{\Delta_x T'}{T'} \bar{U} - \frac{U'}{T'} \Delta_x \bar{T} - \frac{\Delta_z T'}{T'} \bar{W} - \frac{W'}{T'} \Delta_z \bar{T} - \bar{\alpha}. \quad (\text{A4})$$

For the advective terms, each prime variable is evaluated and then composited over six El Niño peaks, averaging from 1 month before to 1 month after each peak. The bar terms represent the mean seasonal cycle, so they are averaged over 100 years in a given season. The result for each term is an anomaly variable (which is not a function of time, as it represents the average structure of an El Niño event) multiplied by a bar variable (which has a seasonal cycle), giving us the seasonality of ENSO growth rates.

The finite differences are taken over the box studied, for example,  $\Delta_x \bar{T}$  is the temperature difference between 190° and 265°E, and the corresponding  $U'$  is averaged over the box studied.

For the surface flux term,  $\bar{\alpha}$  is calculated as the reciprocal of the anomalous  $T'$  corresponding to an excess 1 W/m<sup>2</sup> of surface fluxes in the relevant region and time of year. In other words, since we can calculate the relationship between the anomalous surface fluxes and  $T'$ , we can solve for  $\bar{\alpha}$  by dividing the anomalous surface fluxes by the anomalous temperature of the region studied.

This energy budget is based on the Bjerknes index technique developed in Jin et al. (2006). More specifically, the real part of the Bjerknes index (Re[BI]), which represents growth or decay, depends on the coefficients of the East Pacific temperature and the West Pacific thermocline depth in the differential equations for those variables (i.e.,  $\text{Re}[\text{BI}] \sim R + \epsilon$ , where  $R \approx \frac{1}{T'} \frac{dT'}{dt}$  and  $\epsilon \approx \frac{1}{h_w} \frac{dh_w}{dt}$ , ignoring the phase transition terms from Equations 6.1–6.3 in Jin et al. (2020)). Here, we use a simplified version of each term and focus on those that have been previously shown to be important (Chen & Jin, 2022; Tziperman et al., 1997).

We diagnose  $\epsilon$  directly from the simulations using the following process. First, the West Pacific thermocline depth is defined as the depth with a temperature 4° colder than the surface (results are insensitive to the exact value chosen). Then, the seasonal cycle is removed, and the line of best fit between this anomalous thermocline depth and its time derivative is calculated in each season. This allows for a numerical calculation of  $\epsilon$  in the equation  $dh_w/dt = -\epsilon h_w$ .

The resulting growth rates from the advective terms, surface fluxes, and thermocline relaxation are shown in Figure 5, with the meridional advection terms included in the total growth rate for completeness.

Note that the technique of calculating growth rates fails when  $T'$  is exactly zero, as exponential growth does not make sense at this time. Our technique should therefore be applied only once an El Niño or La Niña event has begun and is growing or decaying; it cannot capture the transition between El Niño and La Niña events. Equivalently, we are examining the real component of the Bjerknes index only, as we wish to understand why ENSO events peak in winter, and we are not concerned with the phase transition of ENSO.

## Data Availability Statement

Reanalysis data used in this study is available from the Climate Data Store (Hersbach et al., 2023). The code for the MITgcm continent simulation is available at [https://github.com/MITgcm/verification\\_other/tree/master/cpl\\_gray%2Bswamp%2Bocn](https://github.com/MITgcm/verification_other/tree/master/cpl_gray%2Bswamp%2Bocn).

## References

- Adero, A., Campin, J.-M., Hill, C., & Marshall, J. (2004). Implementation of an atmosphere–ocean general circulation model on the expanded spherical cube. *Monthly Weather Review*, 132(12), 2845–2863. <https://doi.org/10.1175/MWR2823.1>
- An, S.-I., & Jin, F.-F. (2004). Nonlinearity and asymmetry of ENSO. *Journal of Climate*, 17(12), 2399–2412. [https://doi.org/10.1175/1520-0442\(2004\)017<2399:NAAOE>2.0.CO;2](https://doi.org/10.1175/1520-0442(2004)017<2399:NAAOE>2.0.CO;2)
- Baldwin, J. W., Atwood, A. R., Vecchi, G. A., & Battisti, D. S. (2021). Outsize influence of Central American orography on global climate. *AGU Advances*, 2(2), e2020AV000343. <https://doi.org/10.1029/2020AV000343>
- Battisti, D. S., & Sarachik, E. S. (1995). Understanding and predicting ENSO. *Reviews of Geophysics*, 33(S2), 1367–1376. <https://doi.org/10.1029/95RG00933>

## Acknowledgments

P.J. Tuckman, J. Li, J. Marshall, and N. Lutsko were supported by the NSF Grant OCE-2023520. J. Smyth was supported by the NSF atmospheric and geospace sciences postdoctoral research fellowship (award no. 2123372). The authors thank Jean-Michel Campin for his modeling contributions.

- Bellenger, H., Guilyardi, E., Leloup, J., Lengaigne, M., & Vialard, J. (2014). ENSO representation in climate models: From CMIP3 to CMIP5. *Climate Dynamics*, 42(7), 1999–2018. <https://doi.org/10.1007/s00382-013-1783-z>
- Bjerknes, J. (1969). Atmospheric teleconnections from the equatorial Pacific. *Monthly Weather Review*, 97(3), 163–172. [https://doi.org/10.1175/1520-0493\(1969\)097<0163:ATFTEP>2.3.CO;2](https://doi.org/10.1175/1520-0493(1969)097<0163:ATFTEP>2.3.CO;2)
- Boos, W. R., & Korty, R. L. (2016). Regional energy budget control of the intertropical convergence zone and application to mid-Holocene rainfall. *Nature Geoscience*, 9(12), 892–897. <https://doi.org/10.1038/ngeo2833>
- Burgers, G., Jin, F.-F., & van Oldenborgh, G. J. (2005). The simplest ENSO recharge oscillator. *Geophysical Research Letters*, 32(13), L13706. <https://doi.org/10.1029/2005GL022951>
- Byrne, M. P., & O’Gorman, P. A. (2013). Land–Ocean warming contrast over a wide range of climates: Convective quasi-equilibrium theory and idealized simulations. *Journal of Climate*, 26(12), 4000–4016. <https://doi.org/10.1175/JCLI-D-12-00262.1>
- Chang, P. (1994). A study of the seasonal cycle of sea surface temperature in the tropical Pacific Ocean using reduced gravity models. *Journal of Geophysical Research*, 99(C4), 7725–7741. <https://doi.org/10.1029/93JC03561>
- Chen, H.-C., & Jin, F.-F. (2020). Fundamental behavior of ENSO phase locking. *Journal of Climate*, 33(5), 1953–1968. <https://doi.org/10.1175/JCLI-D-19-0264.1>
- Chen, H.-C., & Jin, F.-F. (2022). Dynamics of ENSO phase-locking and its biases in climate models. *Geophysical Research Letters*, 49(3), e2021GL097603. <https://doi.org/10.1029/2021GL097603>
- Chiang, J. C. H., & Broccoli, A. J. (2023). A role for orbital eccentricity in Earth’s seasonal climate. *Geoscience Letters*, 10(1), 58. <https://doi.org/10.1186/s40562-023-00313-7>
- Clarke, A. J. (2014). El Niño physics and El Niño predictability. *Annual Review of Marine Science*, 6(1), 79–99. <https://doi.org/10.1146/annurev-marine-010213-135026>
- Clement, A. C., Seager, R., & Murtugudde, R. (2005). Why are there tropical warm pools? *Journal of Climate*, 18(24), 5294–5311. <https://doi.org/10.1175/JCLI3582.1>
- Delecluse, P., Davey, M. K., Kitamura, Y., Philander, S. G. H., Suarez, M., & Bengtsson, L. (1998). Coupled general circulation modeling of the tropical Pacific. *Journal of Geophysical Research*, 103(C7), 14357–14373. <https://doi.org/10.1029/97JC02546>
- DeWitt, D. G., & Schneider, E. K. (1999). The processes determining the annual cycle of equatorial sea surface temperature: A coupled general circulation model perspective. *Monthly Weather Review*, 127(3), 381–395. [https://doi.org/10.1175/1520-0493\(1999\)127<0381:TPDTAC>2.0.CO;2](https://doi.org/10.1175/1520-0493(1999)127<0381:TPDTAC>2.0.CO;2)
- Duan, W., & Wei, C. (2013). The ‘spring predictability barrier’ for ENSO predictions and its possible mechanism: Results from a fully coupled model. *International Journal of Climatology*, 33(5), 1280–1292. <https://doi.org/10.1002/joc.3513>
- Erb, M. P., Broccoli, A. J., Graham, N. T., Clement, A. C., Wittenberg, A. T., & Vecchi, G. A. (2015). Response of the equatorial Pacific seasonal cycle to orbital forcing. *Journal of Climate*, 28(23), 9258–9276. <https://doi.org/10.1175/JCLI-D-15-0242.1>
- Frierson, D. M. W., Held, I. M., & Zurita-Gotor, P. (2007). A gray-radiation aquaplanet moist GCM. Part II: Energy transports in altered climates. *Journal of the Atmospheric Sciences*, 64(5), 1680–1693. <https://doi.org/10.1175/JAS3913.1>
- Gaspar, P., Grégoris, Y., & Lefevre, J.-M. (1990). A simple eddy kinetic energy model for simulations of the oceanic vertical mixing: Tests at station Papa and long-term upper ocean study site. *Journal of Geophysical Research*, 95(C9), 16179–16193. <https://doi.org/10.1029/JC095iC09p16179>
- Green, B., Marshall, J., & Donohoe, A. (2017). Twentieth century correlations between extratropical SST variability and ITCZ shifts. *Geophysical Research Letters*, 44(17), 9039–9047. <https://doi.org/10.1002/2017GL075044>
- Guilyardi, E. (2006). El Niño–mean state–seasonal cycle interactions in a multi-model ensemble. *Climate Dynamics*, 26(4), 329–348. <https://doi.org/10.1007/s00382-005-0084-6>
- Guilyardi, E., Wittenberg, A., Fedorov, A., Collins, M., Wang, C., Capotondi, A., et al. (2009). Understanding El Niño in ocean–Atmosphere general circulation models: Progress and challenges. *Bulletin of the American Meteorological Society*, 90(3), 325–340. <https://doi.org/10.1175/2008BAMS2387.1>
- Hersbach, H., Bell, B., Berrisford, P., Biavati, G., Horányi, A., Muñoz Sabater, J., et al. (2023). ERA5 monthly averaged data on single levels from 1940 to present. Copernicus Climate Change Service (C3S) Climate Data Store (CDS). <https://doi.org/10.24381/cds.fi7050d7>
- Hersbach, H., Bell, B., Berrisford, P., Hirahara, S., Horányi, A., Muñoz-Sabater, J., et al. (2020). The ERA5 global reanalysis. *Quarterly Journal of the Royal Meteorological Society*, 146(730), 1999–2049. <https://doi.org/10.1002/qj.3803>
- Hoerling, M. P., Kumar, A., & Zhong, M. (1997). El Niño, La Niña, and the nonlinearity of their teleconnections. *Journal of Climate*, 10(8), 1769–1786. [https://doi.org/10.1175/1520-0442\(1997\)010<1769:ENOLNA>2.0.CO;2](https://doi.org/10.1175/1520-0442(1997)010<1769:ENOLNA>2.0.CO;2)
- Jin, F.-F. (1998). A simple model for the Pacific cold tongue and ENSO. *Journal of the Atmospheric Sciences*, 55(14), 2458–2469. [https://doi.org/10.1175/1520-0469\(1998\)055<2458:ASMFTP>2.0.CO;2](https://doi.org/10.1175/1520-0469(1998)055<2458:ASMFTP>2.0.CO;2)
- Jin, F.-F., Chen, H.-C., Zhao, S., Hayashi, M., Karamperidou, C., Stuecker, M. F., et al. (2020). Simple ENSO models. In *El Niño Southern Oscillation in a Changing Climate* (pp. 119–151). American Geophysical Union (AGU). <https://doi.org/10.1002/9781119548164.ch6>
- Jin, F.-F., Kim, S. T., & Bejarano, L. (2006). A coupled-stability index for ENSO. *Geophysical Research Letters*, 33(23), L23708. <https://doi.org/10.1029/2006GL027221>
- Johnson, G. C., & Birnbaum, A. N. (2017). As El Niño builds, Pacific Warm Pool expands, ocean gains more heat. *Geophysical Research Letters*, 44(1), 438–445. <https://doi.org/10.1002/2016GL071767>
- Kim, S.-K., & An, S.-I. (2021). Seasonal gap theory for ENSO phase locking. *Journal of Climate*, 34(14), 5621–5634. <https://doi.org/10.1175/JCLI-D-20-0495.1>
- Kim, S. T., Yu, J.-Y., & Lu, M.-M. (2012). The distinct behaviors of Pacific and Indian Ocean warm pool properties on seasonal and interannual time scales. *Journal of Geophysical Research*, 117(D5), D05128. <https://doi.org/10.1029/2011JD016557>
- Köberle, C., & Philander, S. G. H. (1994). On the processes that control seasonal variations of sea surface temperatures in the tropical Pacific Ocean. *Tellus A*, 46(4), 481–496. <https://doi.org/10.1034/j.1600-0870.1994.00011.x>
- Levine, A. F. Z., & McPhaden, M. J. (2015). The annual cycle in ENSO growth rate as a cause of the spring predictability barrier. *Geophysical Research Letters*, 42(12), 5034–5041. <https://doi.org/10.1002/2015GL064309>
- Li, T., & Philander, S. G. H. (1996). On the annual cycle of the eastern equatorial Pacific. *Journal of Climate*, 9(12), 2986–2998. [https://doi.org/10.1175/1520-0442\(1996\)009<2986:OTACOT>2.0.CO;2](https://doi.org/10.1175/1520-0442(1996)009<2986:OTACOT>2.0.CO;2)
- Liu, M., Ren, H.-L., Zhang, R., Ineson, S., & Wang, R. (2021). ENSO phase-locking behavior in climate models: From CMIP5 to CMIP6. *Environmental Research Communications*, 3(3), 031004. <https://doi.org/10.1088/2515-7620/abf295>
- Lu, Z., & Liu, Z. (2019). Orbital modulation of ENSO seasonal phase locking. *Climate Dynamics*, 52(7), 4329–4350. <https://doi.org/10.1007/s00382-018-4382-1>

- Marshall, J., Adcroft, A., Hill, C., Perelman, L., & Heisey, C. (1997). A finite-volume, incompressible Navier Stokes model for studies of the ocean on parallel computers. *Journal of Geophysical Research*, *102*(C3), 5753–5766. <https://doi.org/10.1029/96JC02775>
- Marshall, J., Donohoe, A., Ferreira, D., & McGee, D. (2014). The ocean's role in setting the mean position of the Inter-Tropical Convergence Zone. *Climate Dynamics*, *42*(7), 1967–1979. <https://doi.org/10.1007/s00382-013-1767-z>
- Mayer, J., Mayer, M., & Haimberger, L. (2022). *Mass-consistent atmospheric energy and moisture budget data from 1979 to present derived from ERA5 reanalysis, v1.0*. Copernicus Climate Change Service (C3S) Climate Data Store (CDS). <https://doi.org/10.24381/cds.c2451f6b>
- Moreno-Chamorro, E., Marshall, J., & Delworth, T. L. (2020). Linking ITCZ migrations to the AMOC and north Atlantic/Pacific SST decadal variability. *Journal of Climate*, *33*(3), 893–905. <https://doi.org/10.1175/JCLI-D-19-0258.1>
- Neelin, J. D., Chou, C., & Su, H. (2003). Tropical drought regions in global warming and El Niño teleconnections. *Geophysical Research Letters*, *30*(24), 2275. <https://doi.org/10.1029/2003GL018625>
- Philander, S. G. H., Gu, D., Lambert, G., Li, T., Halpern, D., Lau, N.-C., & Pacanowski, R. C. (1996). Why the ITCZ is mostly north of the equator. *Journal of Climate*, *9*(12), 2958–2972. [https://doi.org/10.1175/1520-0442\(1996\)009<2958:WTIMN>2.0.CO;2](https://doi.org/10.1175/1520-0442(1996)009<2958:WTIMN>2.0.CO;2)
- Philander, S. G. H., Pacanowski, R. C., Lau, N.-C., & Nath, M. J. (1992). Simulation of ENSO with a global atmospheric GCM coupled to a high-resolution, tropical Pacific Ocean GCM. *Journal of Climate*, *5*(4), 308–329. [https://doi.org/10.1175/1520-0442\(1992\)005<0308:SOEWAG>2.0.CO;2](https://doi.org/10.1175/1520-0442(1992)005<0308:SOEWAG>2.0.CO;2)
- Philander, S. G. H., Yamagata, T., & Pacanowski, R. C. (1984). Unstable air-sea interactions in the tropics. *Journal of the Atmospheric Sciences*, *41*(4), 604–613. [https://doi.org/10.1175/1520-0469\(1984\)041<0604:UASIT>2.0.CO;2](https://doi.org/10.1175/1520-0469(1984)041<0604:UASIT>2.0.CO;2)
- Schneider, E. K. (2002). Understanding differences between the equatorial Pacific as simulated by two coupled GCMs. *Journal of Climate*, *15*(5), 449–469. [https://doi.org/10.1175/1520-0442\(2002\)015<0449:UDBTEP>2.0.CO;2](https://doi.org/10.1175/1520-0442(2002)015<0449:UDBTEP>2.0.CO;2)
- Schneider, N., Barnett, T., Latif, M., & Stockdale, T. (1996). Warm pool physics in a coupled GCM. *Journal of Climate*, *9*(1), 219–239. [https://doi.org/10.1175/1520-0442\(1996\)009<0219:WPPIAC>2.0.CO;2](https://doi.org/10.1175/1520-0442(1996)009<0219:WPPIAC>2.0.CO;2)
- Stein, K., Timmermann, A., Schneider, N., Jin, F.-F., & Stuecker, M. F. (2014). ENSO seasonal synchronization theory. *Journal of Climate*, *27*(14), 5285–5310. <https://doi.org/10.1175/JCLI-D-13-00525.1>
- Takahashi, K., & Battisti, D. S. (2007a). Processes controlling the mean tropical Pacific precipitation pattern. Part I: The Andes and the eastern Pacific ITCZ. *Journal of Climate*, *20*(14), 3434–3451. <https://doi.org/10.1175/JCLI4198.1>
- Takahashi, K., & Battisti, D. S. (2007b). Processes controlling the mean tropical Pacific precipitation pattern. Part II: The SPCZ and the southeast Pacific dry zone. *Journal of Climate*, *20*(23), 5696–5706. <https://doi.org/10.1175/2007JCLI1656.1>
- Tian, B., Ren, H.-L., Jin, F.-F., & Stuecker, M. F. (2019). Diagnosing the representation and causes of the ENSO persistence barrier in CMIP5 simulations. *Climate Dynamics*, *53*(3), 2147–2160. <https://doi.org/10.1007/s00382-019-04810-4>
- Timmermann, A., An, S.-I., Kug, J.-S., Jin, F.-F., Cai, W., Capotondi, A., et al. (2018). El Niño–southern oscillation complexity. *Nature*, *559*(7715), 535–545. <https://doi.org/10.1038/s41586-018-0252-6>
- Tuckman, P. J., Smyth, J., Lutsko, N. J., & Marshall, J. (2024). The zonal seasonal cycle of tropical precipitation: Introducing the Indo-Pacific monsoonal mode. *Journal of Climate*, *37*(14), 3807–3824. <https://doi.org/10.1175/JCLI-D-23-0125.1>
- Tziperman, E., Zebiak, S. E., & Cane, M. A. (1997). Mechanisms of seasonal – ENSO interaction. *Journal of the Atmospheric Sciences*, *54*(1), 61–71. [https://doi.org/10.1175/1520-0469\(1997\)054<0061:MOSEI>2.0.CO;2](https://doi.org/10.1175/1520-0469(1997)054<0061:MOSEI>2.0.CO;2)
- Vallis, G. K. (1988). Conceptual models of El Niño and the southern oscillation. *Journal of Geophysical Research*, *93*(C11), 13979–13991. <https://doi.org/10.1029/JC093iC11p13979>
- Wang, W., & McPhaden, M. J. (1999). The surface-layer heat balance in the equatorial Pacific ocean. Part I: Mean seasonal cycle. *Journal of Physical Oceanography*, *29*(8), 1812–1831. [https://doi.org/10.1175/1520-0485\(1999\)029<1812:TSLHBI>2.0.CO;2](https://doi.org/10.1175/1520-0485(1999)029<1812:TSLHBI>2.0.CO;2)
- Wang, Y., Wu, R., & Wen, Z. (2019). Seasonal variations in size and intensity of the Indo-western Pacific warm pool in different sectors. *Journal of Oceanography*, *75*(5), 423–439. <https://doi.org/10.1007/s10872-019-00511-y>
- Yin, Z., Dong, Q., Kong, F., Cao, D., & Long, S. (2020). Seasonal and interannual variability of the Indo-Pacific warm pool and its associated climate factors based on remote sensing. *Remote Sensing*, *12*(7), 1062. <https://doi.org/10.3390/rs12071062>
- Yu, X., & McPhaden, M. J. (1999). Seasonal variability in the equatorial Pacific. *Journal of Physical Oceanography*, *29*(5), 925–947. [https://doi.org/10.1175/1520-0485\(1999\)029<0925:SVITEP>2.0.CO;2](https://doi.org/10.1175/1520-0485(1999)029<0925:SVITEP>2.0.CO;2)
- Zebiak, S. E., & Cane, M. A. (1987). A model El Niño–southern oscillation. *Monthly Weather Review*, *115*(10), 2262–2278. [https://doi.org/10.1175/1520-0493\(1987\)115<2262:AMENO>2.0](https://doi.org/10.1175/1520-0493(1987)115<2262:AMENO>2.0)
- Zhou, Z.-Q., Xie, S.-P., Zheng, X.-T., Liu, Q., & Wang, H. (2014). Global warming–Induced changes in El Niño teleconnections over the North Pacific and North America. *Journal of Climate*, *27*(24), 9050–9064. <https://doi.org/10.1175/JCLI-D-14-00254.1>